

Neural network–based closure models for large–eddy simulations with explicit filtering

Mark Benjamin and Gianluca Iaccarino

Center for Turbulence Research, 481 Panama Mall, Stanford, CA 94305

September 2, 2024

Abstract

Data from direct numerical simulations of turbulent flows are commonly used to train neural network–based models as subgrid closures for large–eddy simulations; however, models with low *a priori* accuracy have been observed to fortuitously provide better *a posteriori* results than models with high *a priori* accuracy. This anomaly can be traced to a dataset shift in the learning problem, arising from inconsistent filtering in the training and testing stages. We propose a resolution to this issue that uses explicit filtering of the nonlinear advection term in the large–eddy simulation momentum equations, to control aliasing errors. Within the context of explicitly–filtered large–eddy simulations, we develop neural network–based models for which *a priori* accuracy is a good predictor of *a posteriori* performance. We evaluate the proposed method in a large–eddy simulation of a turbulent flow in a plane channel at $Re_\tau = 180$. Our findings show that an explicitly–filtered large–eddy simulation with a filter–to–grid ratio of 2 sufficiently controls the numerical errors so as to allow for accurate and stable simulations.

1 Motivation

1.1 The closure problem in LES

Large–eddy simulations (LES) are becoming commonplace in the numerical simulation of turbulent flows as a tool for predictive science and engineering. Advances in high–performance computing, numerical methods, and computer hardware have enabled the use of LES in solving complex engineering problems, such as aircraft design [16] and natural ventilation in urban landscapes [20]. The primary modeling challenge in LES is the closure problem for the residual stresses, and the traditional approach relies on using information from the resolved scales. The most commonly–used models, such as the dynamic model [14], leverage scale similarity in the inertial subrange [23]. However, the scale similarity assumption breaks down under a variety of conditions, including ones common in engineering applications such as highly anisotropic turbulence, non–equilibrium turbulence, and moderate Reynolds numbers [35]. The limited success of models that use simple, local algebraic representations of residual stresses in terms of resolved flow scales has led to an interest in more general approaches relying on machine learning (ML) — chiefly, artificial neural networks — to solve the closure problem.

1.2 Neural networks for LES

The present summer of artificial intelligence [38] has seen a considerable increase in efforts that employ machine learning techniques to solve problems in fluid mechanics [7], including turbulence modeling [12]. Increasing availability of high–fidelity numerical simulation data provides fertile ground for using these datasets for training machine learning models for turbulence. While ML has seen more development in Reynolds–averaged Navier–Stokes (RANS) simulations, its use in LES is rapidly gaining prominence. In the present work, we focus on machine learning–based subgrid stress (SGS) models that use neural networks to learn a functional form for the dependence of the SGS stress (or its divergence, the subgrid force) on resolved

quantities that are computable in the simulation, such as the resolved strain rate. This is a supervised learning problem that requires training data with pairs of input features (the aforementioned resolved quantities) and the “true” subgrid stresses in different flow states, which are typically obtained by filtering DNS data. These models are then applied in the same way as traditional models: the networks receive resolved quantities as inputs, and predict the subgrid stress in each grid point and at each time step of the simulation. There have been approaches proposed in the literature that leverage differentiable solvers to provide ML-based closure models [22] [39]; in the present work, we limit ourselves to models that can be applied in general non-differentiable solvers.

Neural network-based subgrid closures have been studied in homogeneous, isotropic turbulence [43] [44], with the conclusion that neural network-based models perform just as well or better than conventional subgrid models in flows they have been trained on. However, in applying a similar procedure to the problem of turbulent channel flow, Park and Choi [32] observed that models that had low *a priori* accuracy (measured by correlations of the SGS stresses predicted by the networks compared to those obtained from the filtered DNS) showed surprisingly good results in *a posteriori* testing (that is, in LES that used the neural networks in the solution procedure), while models with high correlation coefficients (greater than 0.9) were less accurate; this finding was also reported by Kang *et al.* [21]. These anomalous results are explained by noting that the training procedure used for all these works involves an idealized filtering operation applied to the DNS to assemble the “true” subgrid stresses, which nonetheless makes no appearance in the LES that the models are tested in. Stoffer *et al.* [36] accounted for this fact by training a model that learnt both the subgrid scales as well as a representation of the discretization error in the LES; however, the model was unstable, due to compounding of numerical errors in high-wavenumber modes. It has been found that this dynamical accumulation of errors can be best accounted for by using a multi-step loss function coupled with a differentiable solver [39].

While a similar anomaly between *a priori* and *a posteriori* performance is known to exist in traditional subgrid models [29], the nature of the discrepancy is different in the case of neural network-based models, in that the filtering operation used for the training is different from the one used in the testing, which is an example of *dataset shift* or *joint distribution shift* in machine learning. That is, the distributions of the inputs and outputs to and from the network differ between the *a priori* and *a posteriori* stages. A ramification of this inconsistency is the lack of clarity about the performance of a model without expensive *a posteriori* testing.

The objective of the present investigation is to provide a systematic procedure to eliminate this discrepancy, and to develop neural network-based LES closure models for which the accuracy in the training and the inference stage are correlated. We remark here that the terms “training stage”, “*a priori* analysis” and “offline training” are equivalent and represent the same process; likewise, the terms “inference stage”, “*a posteriori* analysis” and “online training” are equivalent. The first pair of terms is more commonly used in the machine learning community, while the second pair is more popular in the turbulence modeling literature. A more detailed description of what both stages represent is provided in Section 2.

The rest of this paper is organized as follows: Section 2 introduces neural network-based subgrid models and highlights the dataset shift issue in the context of turbulent channel flow. Section 3 describes the classical formulation of explicitly-filtered LES, presents details of the filtering operators for both homogeneous and inhomogeneous directions, and presents a framework for subfilter stress modeling in large-eddy simulations using neural networks. Section 4 discusses the results, both in the offline (*a priori*) mode and in the (*a posteriori*) inference LES. Finally, Section 5 summarizes the contribution of the present work, highlights areas that demonstrate promise and present challenges, and discusses the implications of the developed method.

2 Neural network-based SGS modeling

2.1 Implicitly-filtered LES

The equations for LES of an incompressible, isothermal flow, are

$$\partial_i \bar{u}_i = 0 \tag{1}$$

and

$$\partial_t \bar{u}_i + \partial_j (\bar{u}_i \bar{u}_j) = \partial_j (\nu \partial_j \bar{u}_i) - \partial_i \bar{p} / \rho \quad (2)$$

where the unknowns are the filtered velocities \bar{u}_i and the pressure \bar{p} , and the density ρ and kinematic viscosity ν are known constants. The overbar represents a low-pass filtering operation. The second term on the left-hand side is the non-linear advection term, which is the only term not in terms of the primitive variables \bar{u}_i and \bar{p} . The following decomposition [24] is typically employed to rewrite the non-linear product:

$$\overline{u_i u_j} = \bar{u}_i \bar{u}_j + \tau_{ij}, \quad (3)$$

where τ_{ij} represents subfilter stresses that require modeling. This decomposition gives us an alternative form of Equation 2:

$$\partial_t \bar{u}_i + \partial_j (\bar{u}_i \bar{u}_j) = \partial_j (\nu \partial_j \bar{u}_i) - \partial_i \bar{p} / \rho - \partial_j \tau_{ij}, \quad (4)$$

in which the advection term is now in terms of the primitive filtered velocities. The above equation is typically used in practice and referred to as grid-filtered LES, or implicitly-filtered LES, in which the equations are discretized and time-marched with no explicit application of a filter in the solution procedure. This is because the low-pass effect of common discretization schemes and the grid provides an implicit filter [34]. We remark here that in the literature ILES typically refers to a methodology in which the discretization operators are specifically designed with use as subgrid models in mind [4]. In ILES, τ_{ij} assumes the role of the subgrid stress.

2.2 Training procedure for neural networks

In the present work, we employ Fully Connected Neural Networks (FCNN), a type of artificial neural network composed of multiple layers of interconnected neurons, or trainable parameters. Given an input vector $\mathbf{x} \in \mathbb{R}^n$, the FCNN maps it to an output $\mathbf{y} \in \mathbb{R}^m$, through a series of linear transformations alternating with nonlinear activation functions. Specifically, for each layer l , the intermediate output $\mathbf{a}^{(l)} \in \mathbb{R}^{d_l}$ is computed as:

$$\mathbf{a}^{(l)} = \mathbf{W}^{(l)} \mathbf{a}^{(l-1)} + \mathbf{b}^{(l)},$$

where $\mathbf{W}^{(l)} \in \mathbb{R}^{d_l \times d_{l-1}}$ denotes the weight matrix, $\mathbf{b}^{(l)} \in \mathbb{R}^{d_l}$ is the bias vector, and d_l is the dimension of the layer l . The activation function $\sigma^{(l)}(\cdot)$ is then applied element-wise to the linear output, yielding the activated output $\mathbf{h}^{(l)} = \sigma^{(l)}(\mathbf{a}^{(l)})$. The process is repeated for each layer until the final output $\mathbf{y} = \mathbf{h}^{(L)}$ is produced. The goal of the training is to learn a relationship between the subgrid stress (τ_{ij}) and the resolved strain rate (\bar{S}_{ij})

$$\tau_{ij} \approx F(\bar{S}_{ij}; \Theta), \quad (5)$$

where Θ is the set of learnable parameters in the FCNN. The training procedure of an FCNN involves optimizing the learnable parameters Θ to minimize the discrepancy between the network's output and the target values. This is achieved using a loss function $L(\tau_{ij}, \hat{\tau}_{ij})$, which quantifies the error between the predicted output $\hat{\tau}_{ij} = F(\bar{S}_{ij}; \Theta)$ and the true output τ_{ij} . An optimization algorithm is employed to iteratively update the parameters based on the gradient of the loss function with respect to Θ , until convergence is reached. In the evaluation stage, the network predicts the local-in-time-and-space subgrid stress, which is added to the LES. Figure 8 shows a schematic of the entire training and testing process. The procedure involves two stages (represented in the figure by a dotted box); the first involves the training of the neural network. DNS snapshots are filtered (represented in the figure as a convolution operation with a kernel G) to obtain filtered (or resolved) quantities and residual (or subgrid) quantities, which are used to assemble training pairs for the neural network. The network is then trained, resulting in a set of model parameters (Θ). In the second stage, the trained network is integrated into the LES solver, supplying the subgrid stress at each grid point and in each time step. The third column in the figure represents the proposed approach, involving the inclusion of the same filter G in the online LES, which will be discussed in Section 3.

While the training procedure as described above is in general applicable to any type of flow, it is difficult to make *a priori* assessments of generalizability to untrained problems. In the present work, we focus on the problem of developing models that are performant when the flow parameters in the LES match those

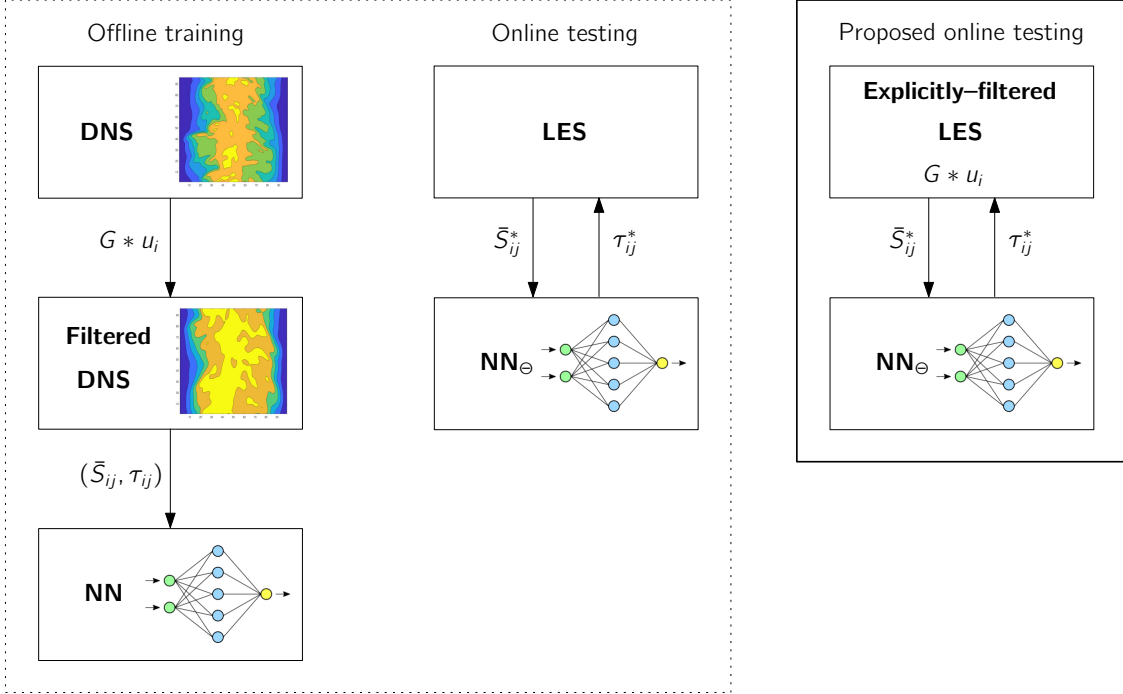


Figure 1: Schematic of the training and testing phases of a neural network–based subgrid model. The filtering operation applied to the training DNS dataset is represented as a convolution of the velocity field u_i with a filter kernel G . The superscript asterisk is used to distinguish quantities computed in the online LES as opposed to obtained from filtered DNS data.

Table 1: Grid details of channel flow direct numerical simulations (DNS) and large–eddy simulations (LES). The grid is uniform in the streamwise (x) and spanwise (z) directions and stretched using a hyperbolic tangent function in the wall–normal direction (y).

	$N_x \times N_y \times N_z$	Δx^+	Δy_{min}^+	Δz^+
DNS	$96 \times 97 \times 96$	11.8	0.1	5.9
LES	$48 \times 48 \times 48$	23.6	0.2	11.8

of the DNS used for the training set, with the understanding that methods developed in the literature for generalization, such as ones involving anisotropic filtering of the training set [33] or transfer learning [17] can be applied on top of the proposed framework.

We consider the turbulent flow in a plane channel at $Re_\tau = 180$ [31]. While this flow is known to have low Reynolds number effects, with a log layer not as well defined as in flows at higher Reynolds numbers, it is nonetheless a useful problem to evaluate a neural network–based method that does not assume the existence of a log law or use near–wall corrections. A second–order, staggered finite difference discretization is used, which solves the LES equations using a pressure projection approach. The convective terms are discretized in the divergence form. Time integration is done using a third–order Runge–Kutta method, which provides a balance between computational cost, storage and the time–accuracy required in scale–resolving simulations. The code has been validated in prior numerical experiments [2]. The flow is driven with a fixed streamwise pressure gradient. The details of the grids for the DNS and the LES are provided in Table 1.

2.3 Accuracy of NN–based SGS models

The accuracy of a neural network–based SGS model depends on the model architecture and the data used for training. Assuming, however, these are optimized by parameter sweeps, there remains the question of poor accuracy due to underfitting from choice of input features. Even with the right choice of network

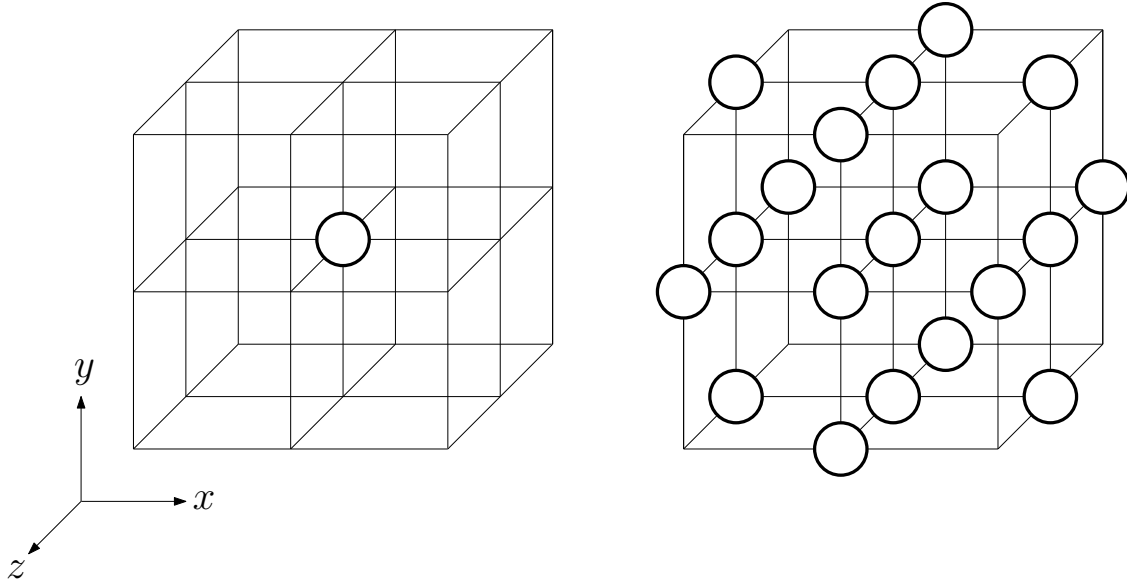


Figure 2: Schematic of the input stencils for the two neural networks in the present study. The circles represent nodes in the structured Cartesian grid. Left: 1-point stencil; right: 19-point stencil. The output of the network in both cases is applied to the central node.

architecture and a substantial and varied dataset, the SGS model may be unable to learn the underlying structure of the SGS stress, leading to a model with low accuracy. While it is common practice to model the SGS stress as a function of the local resolved strain rate, it is known from *a priori* testing that the mapping between these variables is not perfect [10]. In the context of channel flow, it has been observed that the addition of the resolved rotation rate tensor or the pressure gradient has no noticeable effect on the model accuracy [32]. The standard recourse in the literature has been to use strain rate information from neighboring nodes [13] [21] [32] [36] [25], giving non-locality to the model. Alternatively, one might view the information from the adjacent nodes as being equivalent to supplying the network with information about the gradient of the resolved strain rate. In the present work, we build on previous studies carried out in channel flow that determined the number of neighboring grid points required to maximize accuracy [3]. We report results from two models: one that uses local strain rate information (a low-accuracy, 1-point model), and one that uses strain rate information from all neighboring nodes separated by at most two edges (a high-accuracy, 19-point model). A schematic of the input stencils for both models is shown in Figure 2.

Figure 3 (a) shows the results from *a posteriori* testing of both models [3], and shows that the 1-point model predicts the averaged streamwise velocity much better than the 19-point model, which actually performs worse than a simulation that uses no subgrid model at all. As alluded to in Section 2, the discretization error overwhelms the modeling error in ILES at this resolution, and as the networks have not been trained to account for this error, the performance in the inference ILES bears no relation to the accuracy *a priori*. That the good agreement of the 1-point model with the DNS is fortuitous was shown by Benjamin *et al.* [3] by a grid refinement exercise that offset the balancing effect of the discretization error, revealing the “true” poor performance of the model. The velocity fluctuations, shown in Figure 3 (b-d) further support the theory that the match is fortuitous, as the 19-point model is more accurate than the 1-point model in this statistic.

It is clear that models that are agnostic to the discretization scheme in ILES will inevitably suffer from poor predictions due to dataset shift at inference. Two courses of action are possible: the first is to approximate the discretization error in the training data, so that the model learns to account for both modeling and numerical errors simultaneously. This approach has been tried in the literature and found to lead to divergence of the solution [36] [3]; the primary issue therein being that the form of the numerical error poses a harder learning problem than just the SGS stresses. Moreover, adding unbounded forcing terms to the momentum equations has implications for numerical stability of the calculation. Finally, this results in an intimate coupling between the network and the discretization scheme used for the inference LES, which

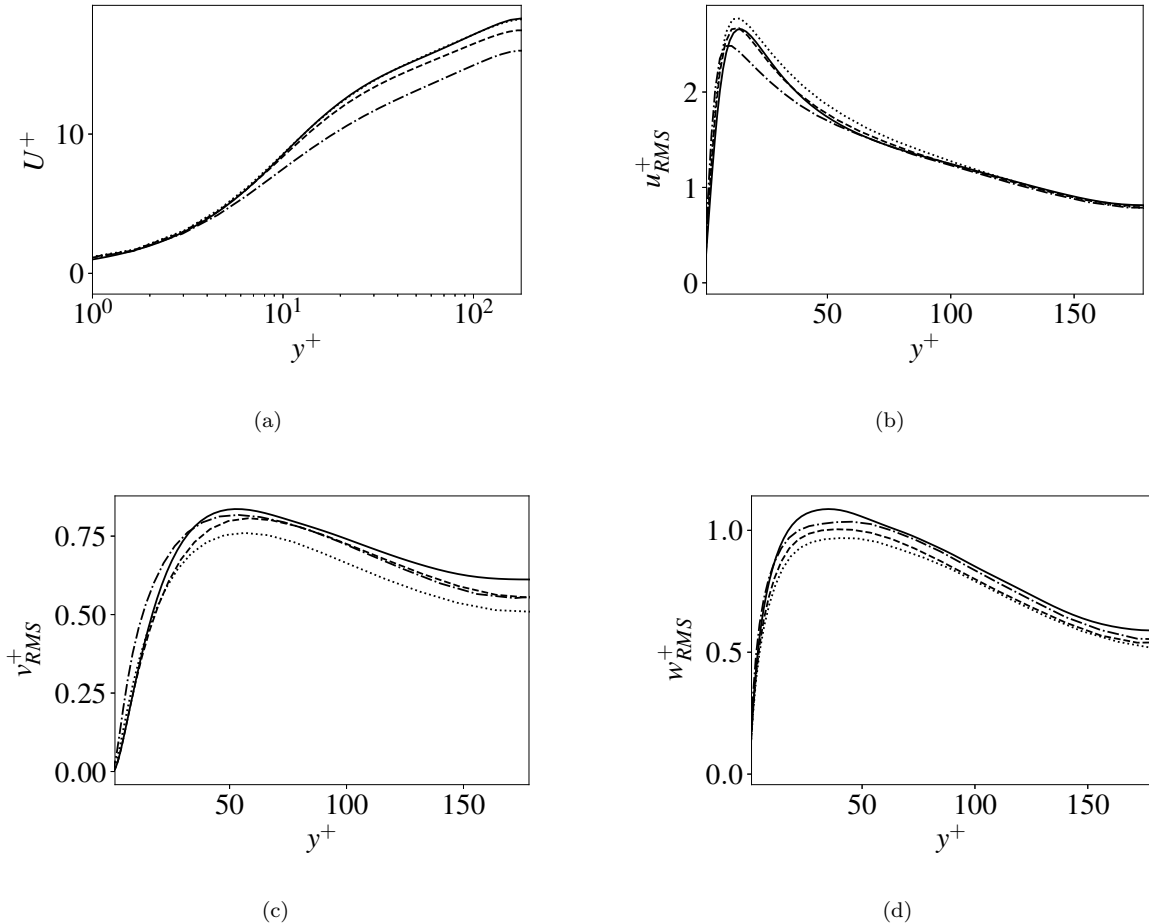


Figure 3: Statistics from ILES: (a) averaged streamwise velocity (U^+) profiles; (b) streamwise velocity fluctuations; (c) wall-normal velocity fluctuations; (d) spanwise velocity fluctuations. Solid line: DNS; dotted line: single-point NN-based model; dashed line: 19-point NN-based model; dot-dashed line: no SGS model.

prevents the model from being used with any other discretization. A network, for instance, trained on the error in a second-order finite difference scheme for the advection term would need retraining before it can be used with a fourth-order finite difference scheme. The alternative is what we propose to do in the present work: to reduce or eliminate completely the numerical error in the solution by explicitly applying the same filter to the inference LES that was used to filter the DNS.

3 Explicitly-filtered LES

The use of an implied filter gives rise to two issues. Firstly, finite difference (or finite volume) operators do not provide a purely low-pass filtering effect [26]. The second is that linking the filtering operation to the grid eliminates the notion of obtaining a grid-converged LES solution. In theory, for a given set of boundary conditions, Equation 4 has a solution that only depends on the choice of filter and subfilter model, when numerical errors have been removed by grid refinement. However, in ILES, grid refinement leads simply to the exposure of smaller scales, a process that only terminates when the Kolmogorov scale for the flow has been resolved. In other words, grid refinement of ILES leads to DNS. The issue with this is that all practical ILES are contaminated with numerical errors, in addition to the modeling errors from the subgrid stress term, and the commingling of both precludes analysis of models independent from the numerical scheme

used for the solution procedure.

An alternative way of solving the LES equations is to apply an explicit filtering operation to the velocities in the simulation. Such simulations (called “explicit” LES, henceforth ELES) typically use the following alternate form of Equation 2:

$$\partial_t \bar{u}_i + \partial_j (\bar{u}_i \bar{u}_j) = \partial_j (\nu \partial_j \bar{u}_i) - \partial_i \bar{p} / \rho - \partial_j \tau_{ij}, \quad (6)$$

which ensures that the frequency content of all the terms in the equation are controlled by the filter, in particular, the advection term.

Although this ELES formulation was advocated already decades ago [30], it has not been commonly used because it was observed that the cost of obtaining a grid-independent ELES was comparable to the cost of a DNS [26]. Moreover, the subfilter models used in ELES performed poorly in comparison with the subgrid models in ILES, even though the two are conceptually similar. There are two reasons for this: the first is that modeling the subfilter scales poses a stiffer challenge than just the subgrid scales, since the filters are larger than the grid, leading to fewer resolved scales and more scales that require modeling. The second reason is that the errors introduced by most numerical schemes used for ILES have a countervailing effect on the modeling error, leading to results in a posteriori simulations that are in general better than one might expect from a priori estimates [15]. At present, explicit filtering is primarily used in the context of approximate deconvolution methods for LES, which attempt to reconstruct the unfiltered velocities from the filtered velocities [37], and in the determination of model coefficients in subgrid models that use the dynamic procedure [14].

3.1 Filtering

For evident reasons, the filter used in LES must attenuate high-frequency signals. A further requirement is that the filter should commute with differentiation, which is an assumption used in arriving at Equations 1 and 2. While this is automatically true of a spatially uniform filter, turbulent flows of interest have directions of inhomogeneity (for instance, due to the presence of a wall), which necessitate the usage of a filter of variable size in order to capture the energy-containing eddies — the premise of large-eddy simulation. To this end, discretely commutative filters have been developed, notably those by Vasilyev *et al.* [41] for non-uniform meshes, with extensions to unstructured meshes [27].

The methodology developed by Vasilyev allows for construction of filters with a commutation error that scales with an arbitrary power of the mesh spacing. Thus, by choosing this power to be equal to or greater than the order of accuracy of the numerical method, the commutation error can be controlled. The filtered velocity in the j th node of a structured, Cartesian grid is obtained as follows:

$$\bar{u}_j = \sum_{l=-K_j}^{L_j} w_l^j u_{j+l}, \quad (7)$$

where w_l^j is the filter weight at the l th location, and K and L form the support of the filter. A three-dimensional filtering is obtained by simply applying this one-dimensional filter recursively in the three directions.

The definition of the filter in physical space is used operationally, as the LES code solves for the velocities in physical space. However, for the filters to consistently attenuate the same scales across different grid resolutions, the transfer function, that is, the Fourier transform associated with the filter:

$$\hat{G}(k) = \sum_{l=-K_j}^{L_j} w_l^j e^{-i\Delta kl}, \quad (8)$$

must be identical for all grids. In addition, while ILES has a single parameter (Δ) that describes both the characteristic grid and filter width, ELES has a grid size (Δ) and a filter size that is typically defined as a multiple m of the grid size ($m\Delta$). Because of this, both the filter size and grid size must be specified in order to ensure the filter behaves consistently as the grid is refined. One may instead choose to specify the grid size and a ratio of the filter size to the grid size, called the Filter-Width Ratio (FWR). Various studies have been

Table 2: Mesh resolution and filter width details for ELES. The grid is uniform in the streamwise (x) and spanwise (z) directions and stretched using a hyperbolic tangent function in the wall-normal direction (y).

Refinement level	Grid resolution	Filter width	Effective resolution
Coarse	48^3	2Δ	24^3
Medium	72^3	3Δ	24^3
Fine	96^3	4Δ	24^3

carried out that demonstrate the relationship between the FWR and the order of accuracy of the numerical method [11] [8] [40]. In this work, we follow the same design of experiments as Bose *et al.* [6], where three grid refinement levels are considered. Figure 4 (a) shows the transfer functions of the filters used in the three different grids; the transfer functions are Gaussian, and of good quality, i.e., there are no overshoots that may spuriously inject energy into the system. We note here that because the filters are not sharp cutoffs in spectral space, we can not apply the filter to the velocity field at the end of a time step; rather, we apply it directly to the non-linear term in the projection step of each iteration, as described in [26]. Figure 4 (b) shows the same transfer functions plotted against a modified wavenumber that accounts for the resolution of the grids they are used in, which shows that, as expected, all filters filter the same physical length scales. The results are shown for the coarsest grid, which matches the computational cost of the ILES (48^3) in terms of degrees of freedom.

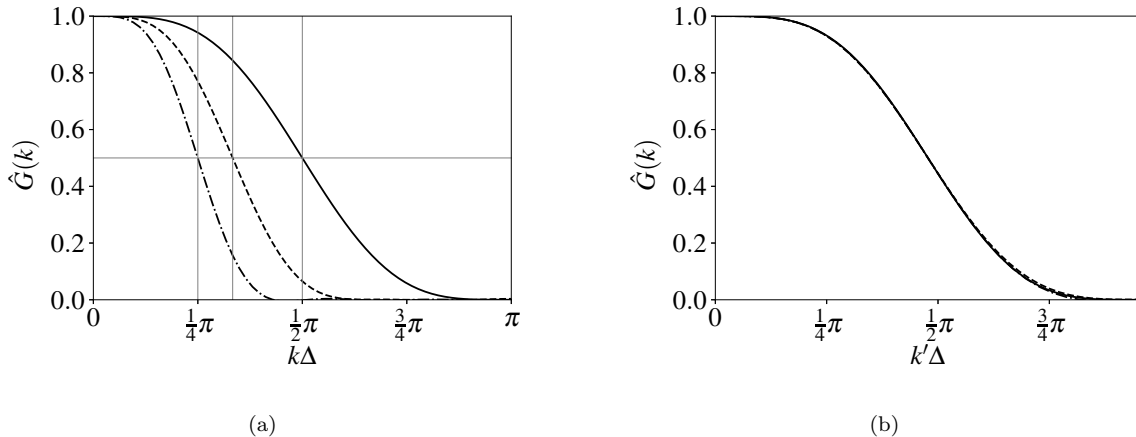


Figure 4: Transfer functions for symmetric, discretely commutative filters of different widths from [6]. Solid line: 2Δ ; dashed line: 3Δ ; dot-dashed line: 4Δ . (a) Transfer functions versus nominal grid size Δ . Cross-hairs indicate nominal filter width. (b) Transfer functions versus scaled grid sizes.

3.1.1 Wall-normal filtering

The channel flow has two periodic, homogeneous directions in which a symmetric filter can be applied. The wall-normal direction, however, requires asymmetric filtering near the wall. These one-sided filters are developed using the quadratic optimization procedure described by Vasilyev [41], which minimizes the differences between the real and imaginary parts of the transfers functions of the asymmetric filter and a symmetric filter of the same width. This approach works reasonably well for the near-wall points, save for the first cell off the wall, which requires a purely one-sided filter. However, for the wall-resolved LES under consideration, this cell is within the viscous sublayer; thus the broadband spectral content of the velocity field is limited and therefore insensitive to the filtering [5]. Thus, no filter is applied at the first cell. Details of the grids used for the ELES are shown in Table 2.

3.1.2 Grid refinement study

We run ELES of the channel at the three grid refinement levels shown above, first with no subfilter model, then with a Smagorinsky subfilter model with a static coefficient, which is known to be inaccurate in wall-bounded flows in the absence of a wall damping function, leading to an over-extended buffer layer, but which we nonetheless show here for demonstrative purposes. Figure 5 (a,b) show the averaged streamwise velocity profiles for the three refinement levels. We see that while the case with no SFS model is converged in the mean velocity at all three refinement levels (the three curves overlap perfectly), while the case with the Smagorinsky model is still not fully converged at the 3Δ level. The latter behavior is expected; analysis of modeling and numerical error by Chow and Moin [15], based on the framework developed by Ghosal [9], recommends a filter width of at least 4Δ for grid-independence of ELES with a second-order finite differences solver. The convergence of the case with no SFS model is attributed to the lack of numerical error introduced by the eddy-viscosity closure. As expected from a simulation with no modeling of the subfilter scales, the converged solution is inaccurate. Similar behavior is seen in the higher order statistics (Figure 5 (c,d)), where the case with the Smagorinsky subfilter model is unconverged, whereas the case with no subfilter model converges at the 3Δ level.

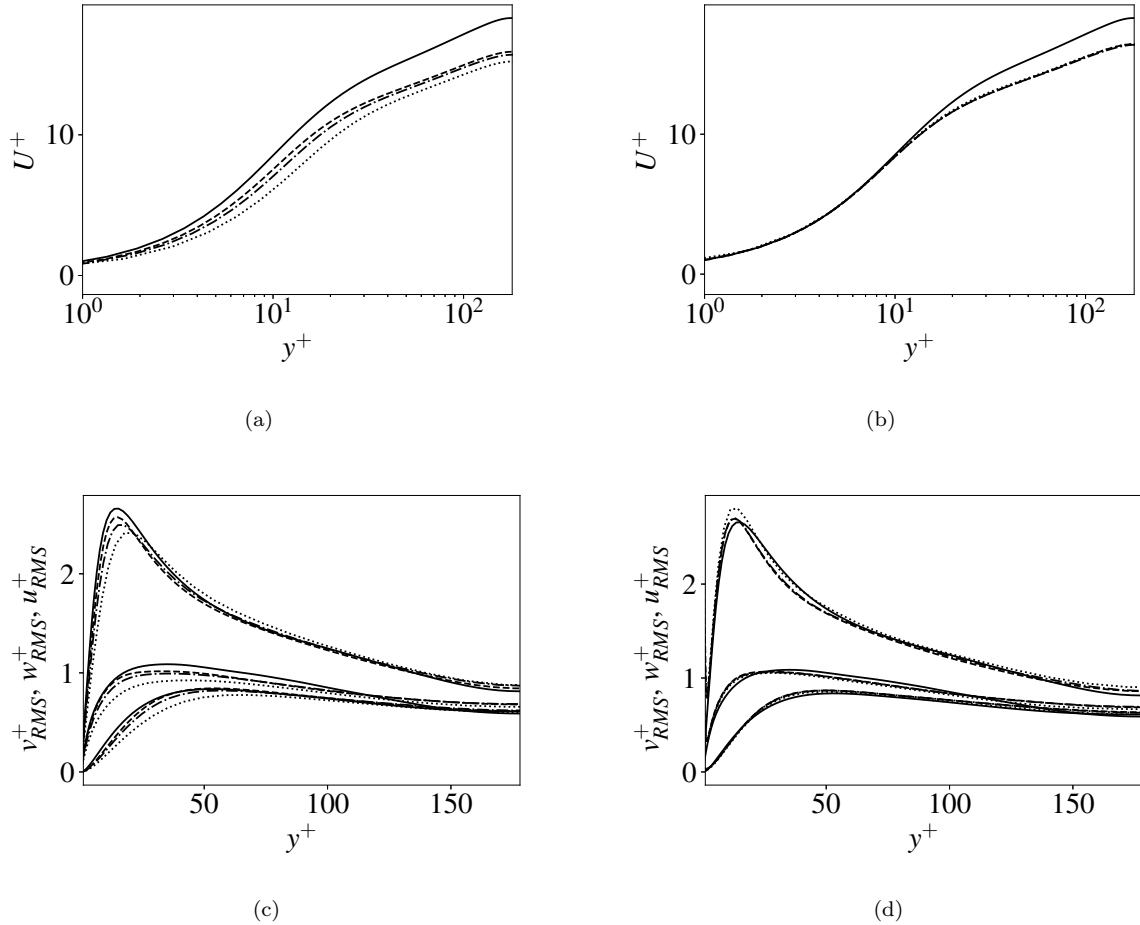


Figure 5: Statistics for ELES: (a) Averaged streamwise velocity (U^+) with static Smagorinsky subfilter model and (b) no subfilter model; (c) Averaged velocity fluctuations with static Smagorinsky subfilter model and (d) no subfilter model. Solid line: DNS; dots: 48^3 grid; dot-dashed line: 72^3 grid; dashed line: 96^3 grid.

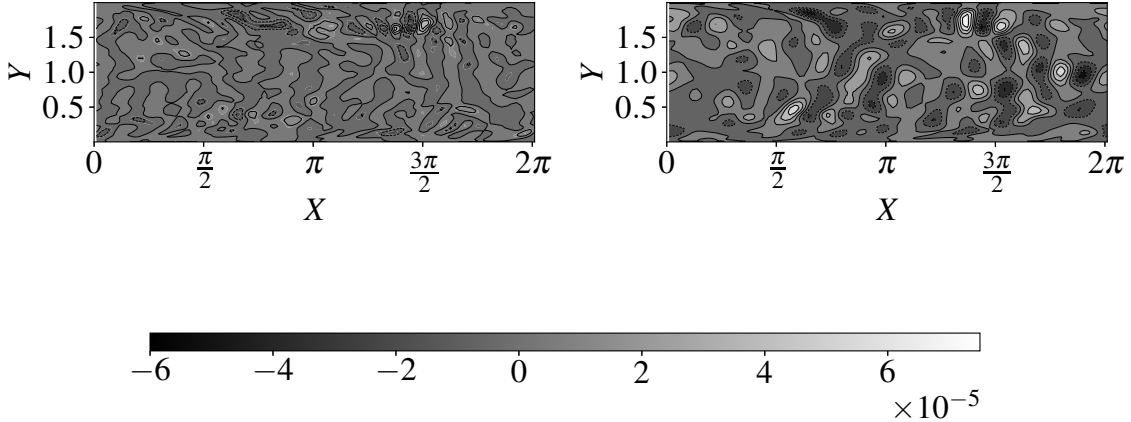


Figure 6: Contours of τ_{12} normalized using wall units, from a spanwise plane of filtered DNS, with isocontour lines overlaid. Left: filtered with a 2Δ filter for the ILES; right: filtered with a 4Δ filter for the ELES.

3.2 Neural networks for ELES

The neural networks for the subfilter stress in ELES are trained in a manner identical to that of ILES (see Section 2.2). As with ILES, two networks are considered: one that uses local strain rate information, and one that uses a 19-point stencil of strain rates. The details of the training procedure are provided in Table 3. Since the neural networks will be called at each grid point and each time step, as described in Section 2, it is crucial to maintain a compact architecture to ensure computational efficiency. The floating-point operations per second (FLOPs) scale with the network’s number of nodes per layer (N_{nodes}) and the number of layers (N_{layers}), and can be estimated as $\mathcal{O}(N_{layers} \times N_{nodes}^2)$, and this can quickly overwhelm the cost of the other terms in the momentum update steps of the pressure-projection scheme. For this reason, we avoid the use of dropout layers [19] in the architecture; given the modest size of the networks, it is more advisable to simply reduce the size of the network, in case of overfitting. The networks are initially sized using the work by Park and Choi [32]. To run the ELES at the same resolution as the ILES (48^3 nodes), we apply a 4Δ filter to the DNS snapshots in the training stage, rather than the 2Δ used for the ILES. Thus, the ELES models need to account for more scales than the equivalent ILES. This is illustrated in Figure 6, which shows contours of τ_{12} at a spanwise plane for the ILES and the ELES. The subfilter model for the ELES has to predict stresses that are not only of a broader range of magnitudes, but also learn a more complex functional form, as there is a natural transfer of information from the filtered and residual quantities, as the size of the filter increases. The limiting size of the filter can be determined from the heuristic that large-eddy simulations should resolve about 75% of the energy in the flow. For the present work, we merely focus on matching the resolution cost of the ILES.

We adopt an eddy-viscosity closure for the subgrid stresses, given by

$$\tau_{ij}^d = -2\nu_t^{NN} \bar{S}_{ij} \quad (9)$$

where ν_t^{NN} is the eddy-viscosity, and τ_{ij}^d represents the deviatoric part of the SFS stress; the trace being absorbed into the pressure field. It is seen that a direct prediction of the subfilter stress or subfilter force by the neural network leads to solutions that diverge [28] [42]; the use of an eddy-viscosity model allows for a natural way of incorporating the impact of the subfilter scales on the resolved scales by modulating the effective viscosity of the flow. To prevent destabilization of the calculations by excessive backscatter, we restrict the eddy-viscosity to positive values by applying a ReLU activation to the output layer. We note here that the choice of closure model — or the decision to predict a turbulent viscosity rather than the

Table 3: Training dataset, network architecture and hyperparameter details for ELES.

Training data	
Dataset	96 ³ DNS instantaneous flow fields
No. of samples	750 fields; every 4th point in x and z ; 41M samples
Filter width	4 Δ
Data non-dimensionalization	Wall units
Network architecture	
Network type	Fully-connected, feed-forward neural network
Network size	2 hidden layers; 32 nodes per layer
Network inputs	Strain rate tensor \bar{S}_{ij}
Network output	Eddy viscosity ν_t
Activation functions	ReLU
Optimization details	
Loss function	Mean squared error
Optimizer	Adam
Learning rate	10 ⁻⁴
Batch size	2048
No. of epochs	250
Input noise	Gaussian; 5% of input magnitude

stresses or their divergence directly — is solely to do with the stability of the inference LES, and does not affect the arguments about the consistency of the filtering between the training and testing phases. Since enforcing positivity of ν_t has the effect of overpredicting the subfilter production term ($\mathcal{P}r = -\tau_{ij}\bar{S}_{ij}$), we rescale the subgrid stresses to maintain the net production in the domain in each training snapshot, following similar approaches in the literature [1] [32]; however, we apply the rescaling at the training stage, rather than the inference stage, to avoid computing domain-averages in each timestep of the simulation. Thus, we first eliminate backscatter:

$$\tau_{ij}^> = \begin{cases} 0, & \text{if } \mathcal{P}r < 0 \\ \tau_{ij}, & \text{otherwise} \end{cases} \quad (10)$$

then rescale the subfilter stresses as follows:

$$\tau_{ij}^* = \tau_{ij}^> \left(\frac{\int \mathcal{P}r \, dV}{\int \mathcal{P}r^> \, dV} \right) \quad (11)$$

where $\mathcal{P}r^> = -\tau_{ij}^>\bar{S}_{ij}$.

4 Model testing

4.1 A priori analysis

The accuracy of the two trained neural networks is measured offline by making predictions on filtered snapshots that were not used for the training. Since the primary goal of a subfilter model is to dissipate the right amount of energy from the resolved scales, we quantify the prediction of the model in terms of the subfilter production term, which appears in the resolved kinetic energy equation. For an eddy-viscosity model, this is given by

$$\mathcal{P}r = 2\nu_t^{NN}\bar{S}_{ij}\bar{S}_{ij}. \quad (12)$$

Figure 7 shows a correlation plot between the subfilter production predicted by the 1-point model ($\mathcal{P}r^{pred}$) and the subfilter production obtained by filtering the DNS ($\mathcal{P}r^{true}$). The Pearson correlation coefficient is 0.85. We see a general tendency of the model to underpredict the subfilter production, from the positive slope of the core of the correlation plot relative to the reference line. Additionally, the marginal probability

densities show that the tail of the distribution is poorly predicted. Figure 8 shows the correlation plot for the 19-point model; the predictions are much better correlated with the truth values, and the tail of the distribution properly captured, with a correlation coefficient of 0.99. Any scatter observable in the plot relative to the reference line occurs with low probability, as seen by the tail of the distribution, which is well-predicted.

4.2 A posteriori analysis

Figure 9 shows the results from the ELES with the two neural network-based SFS models. We see that the single-point model provides too much dissipation and leads to an overprediction of the mass flux. The 19-point model, however, provides a much more accurate prediction, and we observe a convergence towards the DNS, as predicted by the *a priori* correlations. Similar convergence trends are observed in the stresses, with the near-wall peak in the streamwise fluctuations much better predicted by the 19-point model, though it must be noted that these higher order statistics are limited by the linear eddy-viscosity assumption, which tends to overpredict the streamwise stresses at the expense of the other two directions. However, the present framework does not place restrictions upon the form of the closure; as described earlier, a positive eddy-viscosity model is used here for stability, but anisotropic models that do not make assumptions about the alignment between the resolved strain rate tensor and the subfilter tensor can be explored in future work to further improve the accuracy of higher-order statistics.

To assess the extent to which the ELES approach mitigates the dataset shift, Figure 10 plots histograms of the \bar{S}_{12} — the primary component that is active in a plane channel driven along the x -direction — and compares those obtained from the filtered DNS used for training with those obtained from the *a posteriori* LES. We see that when ELES is used, not only do both the single and multi-point models closely approximate the distribution of the DNS, but we again observe convergence with increasing model accuracy; i.e., the 19-point histogram is almost exactly aligned with the DNS. On the other hand, the histograms for ILES clearly demonstrate that the inference simulation does not “see” strain rates drawn from a similar distribution to the ones used for training the models, for both the 1-point and 19-point cases.

In order to study the effect of the explicit filtering on the spectral content of the simulation, we show the streamwise energy spectra at the channel midplane for different simulations in Figure 11, comparing DNS with filtered DNS, the single-point subgrid model from ILES (which is the most accurate in the *a posteriori* test) and the 19-point subfilter model from ELES. We observe that the ELES shows range of scales that is more limited than ILES, and is much closer to the DNS in the tail of the spectrum. The energy in the large scales is unmodified, as is consistent with our expectations. Finally, we note that while the velocity profiles for the single-point subgrid model in ILES matched the DNS, the fact that the spectrum is polluted with high-frequency noise from the numerical error is further evidence that error cancelation is the cause of the seemingly good accuracy. With ELES, we see that the filtering controls the noise in the tail of the spectrum, leaving the accurate network to provide the correct amount of dissipation to match the mean flow statistics.

5 Conclusions

In this work, we begin by highlighting a consistency issue between online and offline training that occurs in state-of-the-art neural network-based methods for subgrid stress closure modeling in LES, clarifying observations made in the literature that highlight the contradictory results stemming from this issue. While this is alternatively explained as a failure to account for LES discretization errors while learning the functional form, it is important to highlight that the networks are faced with a dataset shift, which is what makes them uniquely sensitive to numerical errors in a way that physics-based closures are not.

We then propose a resolution to this inconsistency, by reformulating the problem using explicitly-filtered LES, which allows us to separate the numerical and modeling errors, using explicit filtering of the nonlinear term to control the former, while allowing the networks to account for the latter. We show that although this requires the networks to learn a more complex functional form — since they now have to account for both the subgrid and the subfilter scales — the models now perform consistently with expectations from *a priori* accuracy studies.

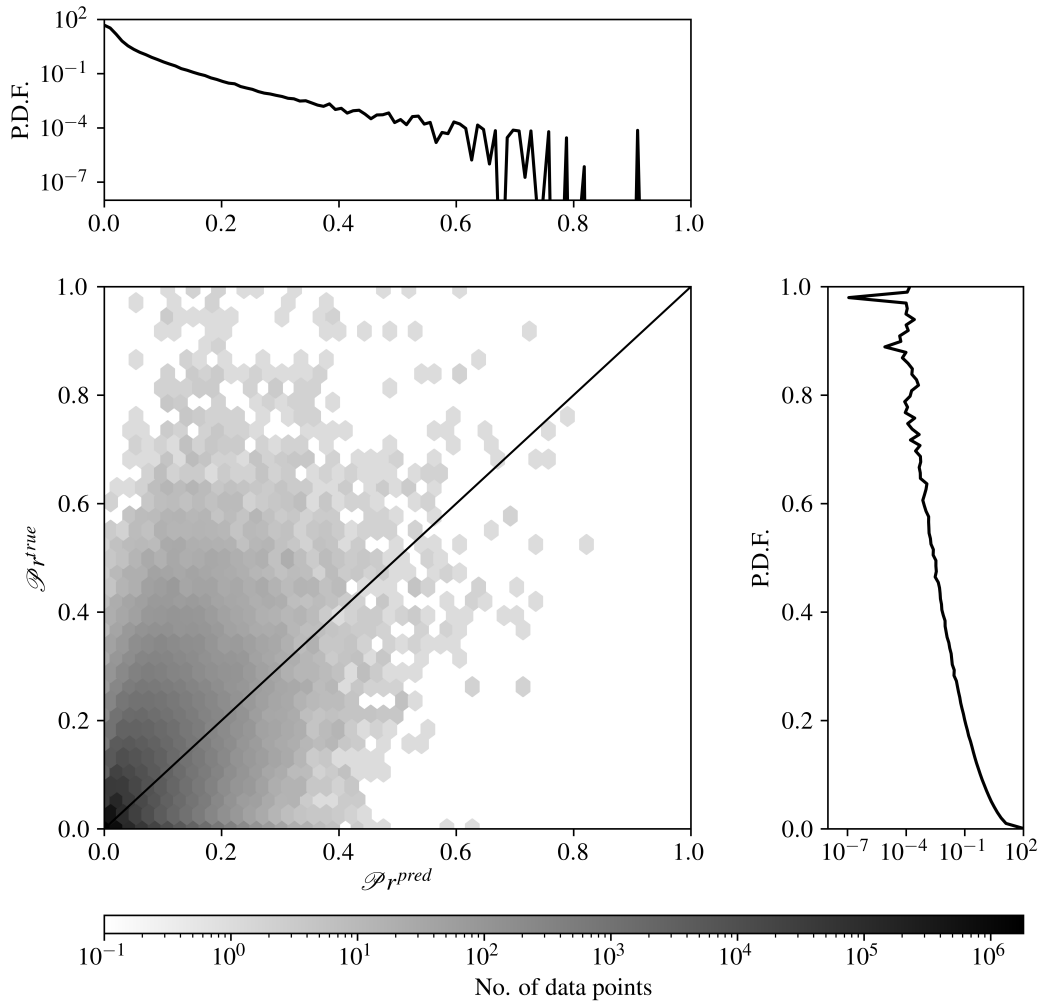


Figure 7: Correlation plot of subgrid production (\mathcal{P}_r^{pred} versus \mathcal{P}_r^{true}) for the 1-point \overline{S}_{ij} subfilter model, with marginal probability density functions (P.D.F.s). Values are normalized by wall scaling. The hexagonal bins are shaded by density. 4 million data points are represented.

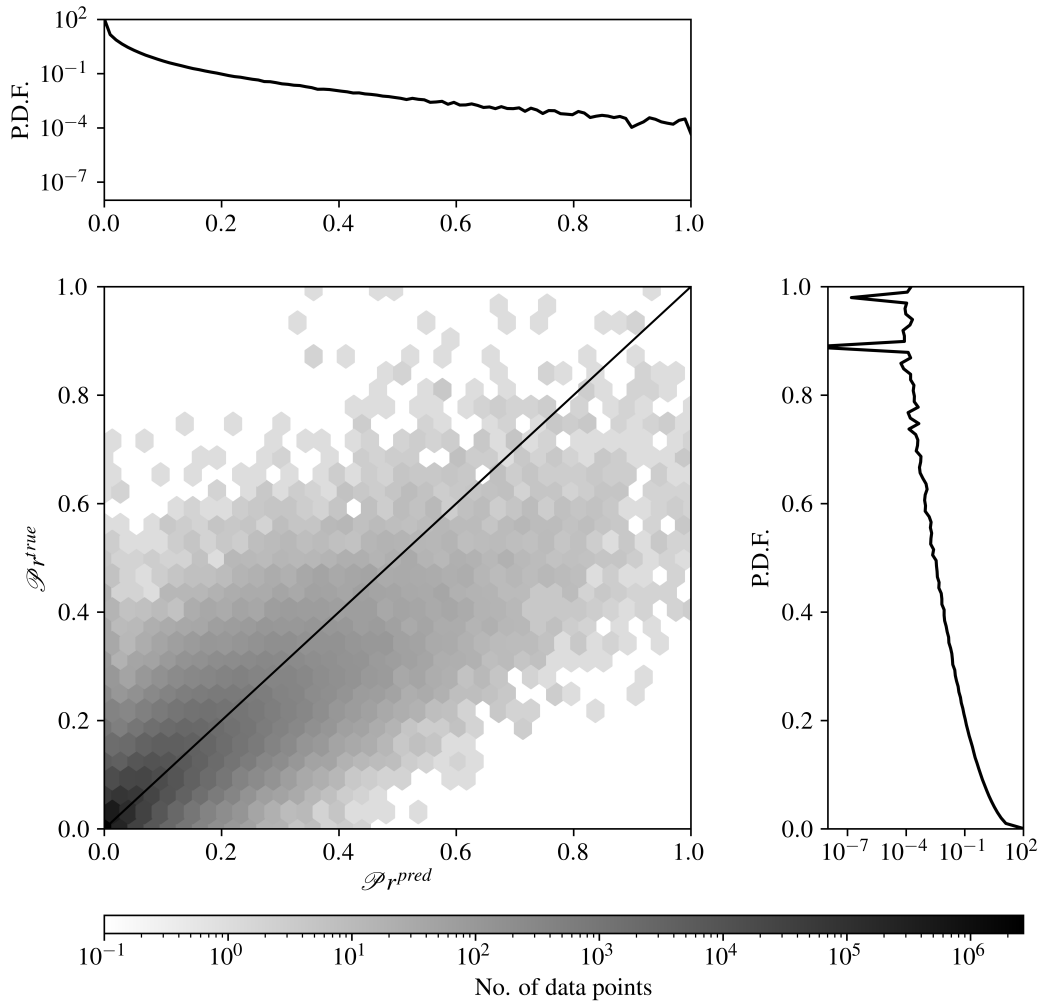


Figure 8: Correlation plot of subgrid production (\mathcal{P}_r^{pred} versus \mathcal{P}_r^{true}) for the 19-point \overline{S}_{ij} subfilter model, with marginal probability density functions (P.D.F.s). Values are normalized by wall scaling. The hexagonal bins are shaded by density. 4 million data points are represented.

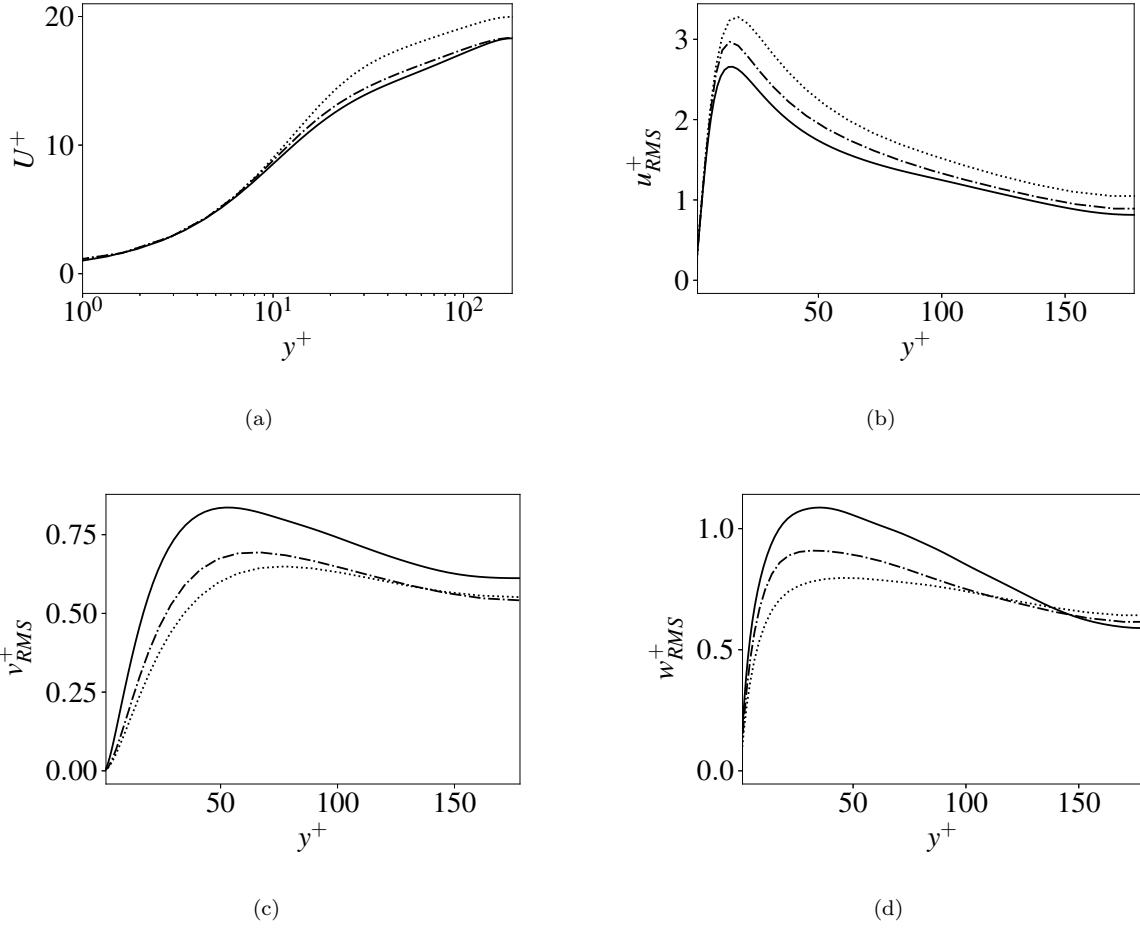


Figure 9: Statistics from ELES: (a) averaged streamwise velocity (U^+) profiles; (b) streamwise velocity fluctuations; (c) wall-normal velocity fluctuations; (d) spanwise velocity fluctuations. Solid line: DNS; dotted line: single-point NN-based model; dashed line: 19-point NN-based model.

While the objective of the present work is not to make detailed comparisons of neural network-based subfilter models with physics-based models for ELES, we note here that the performance of physics-based closure models degrades when the LES is explicitly filtered. The reason for this is twofold: firstly, as mentioned earlier, ELES subfilter models need to account for more scales than the equivalent ILES subgrid models; secondly, some of the inadequacy of subgrid models is masked by numerical dissipation; thus, when this dissipation is controlled by explicit filtering, the “true” performance of the model is observed. For instance, Gullbrand and Chow [18] found that the performance of the dynamic Smagorinsky model in a channel flow degraded significantly when the LES was explicitly filtered relative to when an implicit grid filter was used.

In theory, the approach presented here allows for a neural network-based closure model that has less solver-dependence, which is a key step in developing portable models that do not require expensive offline re-training for use in different solvers.

Acknowledgments

The authors gratefully acknowledge discussions with Sanjeeb Bose, Adrian Lozano-Durán and Stefan Domino.

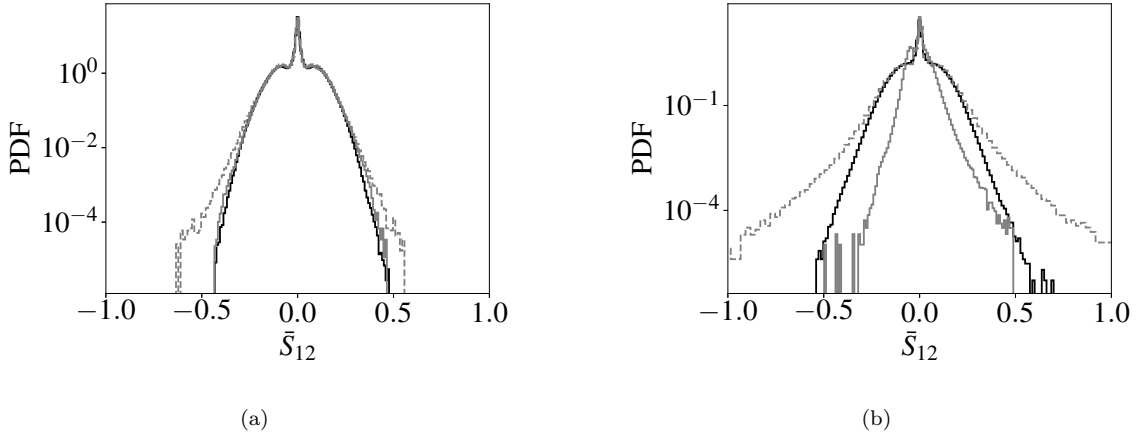


Figure 10: Histograms of \bar{S}_{12} from (a) ELES and (b) ILES. Solid black line: DNS (filtered at 4Δ for ELES and 2Δ for ILES); dashed gray line: 1-pt model; solid gray line: 19-pt model.

Declaration of competing interests

The authors declare that they have no known competing financial interests or personal relationships that could have appeared to influence the work reported in this paper.

Data availability

The data used for training the neural networks as well as that used for generating the plots in this manuscript will be made available upon request.

Appendix A: Grid-independence of single-point SFS models for ELES

In explicitly-filtered LES, the neural network learns a functional form that relates filtered and residual quantities which is dependent only on the choice of filter. This means that absent significant interference from the numerical error in the low filter-to-width ratio simulations, the network should be performant on any grid, provided the same physical scales are filtered in the same way. This is simplest to test using the low-accuracy single-point model, since the non-local 19-point model implicitly includes an additional length scale that introduces grid-dependence (the average distance between each pair of the 19 nodes). Figure 12 shows the streamwise velocity profiles for ELES using the single-point model on the three grids under consideration, and confirms this expectation of grid-independence. This means that while for the sake of accuracy the 19-point model is preferable, there is a benefit to be had from a local model, as the present ELES formulation avoids the need for training on several grids, an approach that is taken with neural network-based models for ILES [32]. The other significant implication of the above result is that we can now use the 48^3 grid for the neural network-based subfilter model, which significantly saves computational cost, and makes the calculations as affordable as the ILES in terms of degrees of freedom.

Appendix B: Spectra of ELES with and without subfilter models

Figure 13 shows the streamwise velocity spectrum at the channel midplane, with a view to comparing the spectra obtained when running ELES with and without a subfilter model. The 19-point ELES SFS model is shown. We see that in the case with no subfilter model, there is an accumulation of energy at the smaller

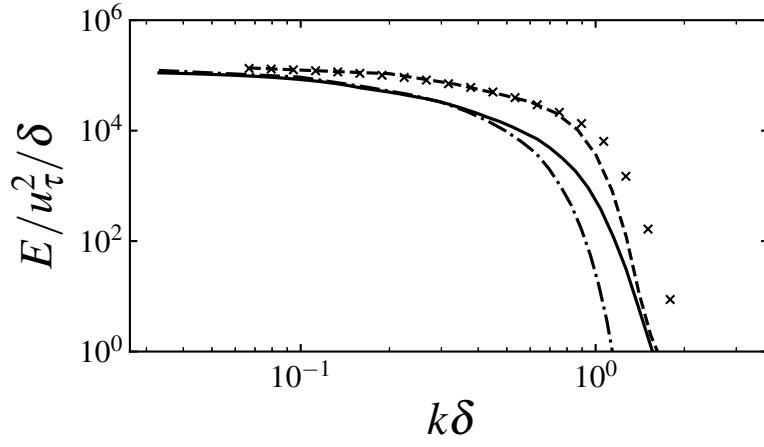


Figure 11: Streamwise velocity spectrum at $y^+ \approx 180$, non-dimensionalized by friction velocity (u_τ) and channel half-height (δ). Solid line: DNS; dot-dashed lines: DNS filtered at 4Δ ; dashed line: ELES with 19-pt model; crosses: ILES with 1-pt model

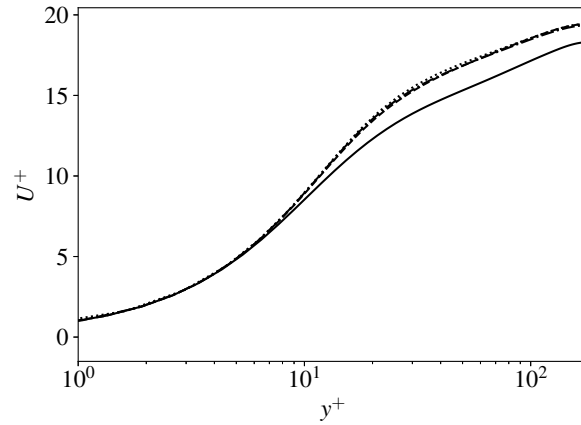


Figure 12: Averaged streamwise velocity (U^+) profiles for the single-point ELES subfilter model. Solid line: DNS; dotted line: 48^3 grid; dot-dashed line: 72^3 grid; dashed line: 96^3 grid.

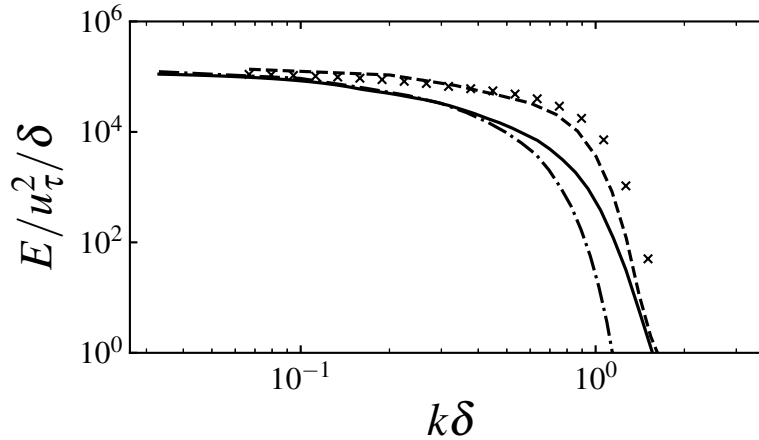


Figure 13: Streamwise velocity spectrum at $y^+ \approx 180$, non-dimensionalized by friction velocity (u_τ) and channel half-height (δ). Solid line: DNS; dot-dashed lines: DNS filtered at 4Δ ; dashed line: ELES with 19-pt model; crosses: ELES with no subfilter model; solid gray line: -1 power law.

scales, at a non-dimensional wavenumber of approximately unity. The neural network-based subfilter model has the effect of drawing energy appropriately from the smallest resolved scales, which is consistent with the role of a subfilter model.

References

- [1] R. Akhavan, A. Ansari, S. Kang, and N. Mangiavacchi. Subgrid-scale interactions in a numerically simulated planar turbulent jet and implications for modelling. *Journal of Fluid Mechanics*, 408:83–120, 2000.
- [2] H. Jane Bae and Adrián Lozano-Durán. Effect of wall boundary conditions on a wall-modeled large-eddy simulation in a finite-difference framework. *Fluids*, 6(3), 2021.
- [3] M. Benjamin, S. Domino, and G. Iaccarino. Challenges in the use of neural networks for large-eddy simulations. *CTR Annual Research Briefs*, pages 123–135, 2022.
- [4] J.P. Boris, F.F. Grinstein, E.S. Oran, and R.L. Kolbe. New insights into large eddy simulation. *Fluid Dynamics Research*, 10(4):199–228, 1992.
- [5] Sanjeeb Bose. Private communication, 2023.
- [6] Sanjeeb T Bose, Parviz Moin, and Donghyun You. Grid-independent large-eddy simulation using explicit filtering. *Physics of Fluids*, 22(10):105103, 2010.
- [7] Steven L Brunton, Bernd R Noack, and Petros Koumoutsakos. Machine learning for fluid mechanics. *Annu. Rev. Fluid Mech.*, 52:477–508, 2020.
- [8] Fotini K Chow and Parviz Moin. Explicit filtering for large eddy simulation on unstructured grids. *Center for Turbulence Research Annual Research Briefs*, pages 3–14, 2005.
- [9] Fotini Katopodes Chow and Parviz Moin. A further study of numerical errors in large-eddy simulations. *Journal of Computational Physics*, 184(2):366–380, 2003.
- [10] Robert A. Clark, Joel H. Ferziger, and W. C. Reynolds. Evaluation of subgrid-scale models using an accurately simulated turbulent flow. *Journal of Fluid Mechanics*, 91(1):1–16, 1979.

- [11] Giuliano De Stefano, Oleg V Vasilyev, and David E Goldstein. Effects of filter type and grid resolution on explicitly filtered large-eddy simulations. *Flow, Turbulence and Combustion*, 74(3):261–284, 2005.
- [12] Karthik Duraisamy, Gianluca Iaccarino, and Heng Xiao. Turbulence modeling in the age of data. *Annu. Rev. Fluid Mech.*, 51:357–377, 2019.
- [13] Masataka Gamahara and Yuji Hattori. Searching for turbulence models by artificial neural network. *Phys. Rev. Fluids*, 2, 2017.
- [14] Massimo Germano, Ugo Piomelli, Parviz Moin, and William H. Cabot. A dynamic subgrid-scale eddy viscosity model. *Phys. Fluids A: Fluid Dynamics*, 3(7):1760–1765, 1991.
- [15] Sandip Ghosal. An analysis of numerical errors in large-eddy simulations of turbulence. *Journal of Computational Physics*, 125(1):187–206, 1996.
- [16] Konrad A Goc, Oriol Lehmkuhl, George Ilhwan Park, Sanjeeb T Bose, and Parviz Moin. Large eddy simulation of aircraft at affordable cost: a milestone in computational fluid dynamics. *Flow*, 1:E14, 2021.
- [17] Yifei Guan, Ashesh Chattopadhyay, Adam Subel, and Pedram Hassanzadeh. Stable a posteriori les of 2d turbulence using convolutional neural networks: Backscattering analysis and generalization to higher *re* via transfer learning. *Journal of Computational Physics*, 458:111090, 2022.
- [18] Jessica Gullbrand and Fotini Katopodes Chow. The effect of numerical errors and turbulence models in large-eddy simulations of channel flow, with and without explicit filtering. *Journal of Fluid Mechanics*, 495:323–341, 2003.
- [19] Geoffrey E Hinton, Nitish Srivastava, Alex Krizhevsky, Ilya Sutskever, and Ruslan Salakhutdinov. Improving neural networks by preventing co-adaptation of feature detectors. *arXiv preprint arXiv:1207.0580*, 2012.
- [20] Yunjae Hwang and Catherine Górlé. Large-eddy simulations to define building-specific similarity relationships for natural ventilation flow rates. *Flow*, 3:E10, 2023.
- [21] Myeongseok Kang, Youngmin Jeon, and Donghyun You. Neural-network-based mixed subgrid-scale model for turbulent flow. *arXiv preprint arXiv:2205.10181*, 2022.
- [22] Dmitrii Kochkov, Jamie A. Smith, Ayya Alieva, Qing Wang, Michael P. Brenner, and Stephan Hoyer. Machine learning–accelerated computational fluid dynamics. *Proceedings of the National Academy of Sciences*, 118(21):e2101784118, 2021.
- [23] Andrei N. Kolmogorov. The local structure of turbulence in incompressible viscous fluid for very large reynolds number. *Dokl. Akad. Nauk. SSSR*, 30:301–303, 1941.
- [24] A. Leonard. Energy cascade in large-eddy simulations of turbulent fluid flows. In F.N. Frenkiel and R.E. Munn, editors, *Turbulent Diffusion in Environmental Pollution*, volume 18 of *Advances in Geophysics*, pages 237–248. Elsevier, 1975.
- [25] Bo Liu, Huiyang Yu, Haibo Huang, Nansheng Liu, and Xiyun Lu. Investigation of nonlocal data-driven methods for subgrid-scale stress modeling in large eddy simulation. *AIP Advances*, 12(6):065129, 2022.
- [26] T.S. Lund. The use of explicit filters in large eddy simulation. *Comput. Math. with Appl.*, 46(4):603–616, 2003. Turbulence Modelling and Simulation.
- [27] Alison L Marsden. Construction of commutative filters for les on unstructured meshes. *Journal of computational physics*, 175(2), 2002.
- [28] R. Maulik, O. San, A. Rasheed, and P. Vedula. Subgrid modelling for two-dimensional turbulence using neural networks. *Journal of Fluid Mechanics*, 858:122–144, 2019.

- [29] Charles Meneveau and Joseph Katz. Scale-invariance and turbulence models for large-eddy simulation. *Annual Review of Fluid Mechanics*, 32(1):1–32, 2000.
- [30] Parviz Moin and John Kim. Numerical investigation of turbulent channel flow. *Journal of Fluid Mechanics*, 118:341–377, 1982.
- [31] Robert Moser, John Kim, and Nagi Mansour. Direct numerical simulation of turbulent channel flow up to $Re=590$. *Phys. Fluids*, 11:943–945, 04 1999.
- [32] Jonghwan Park and Haecheon Choi. Toward neural-network-based large eddy simulation: application to turbulent channel flow. *J. Fluid Mech.*, 914:A16, 2021.
- [33] Aviral Prakash, Kenneth E. Jansen, and John A. Evans. Invariant data-driven subgrid stress modeling in the strain-rate eigenframe for large eddy simulation. *Computer Methods in Applied Mechanics and Engineering*, 399:115457, 2022.
- [34] Robert S. Rogallo and Parviz Moin. Numerical simulation of turbulent flows. *Annual Review of Fluid Mechanics*, 16:99–137, 1984.
- [35] K.R. Sreenivasan. On the universality of the kolmogorov constant. *Physics of Fluids*, 7(11):2778–2784, 1995.
- [36] R. Stoffer, C. M. van Leeuwen, D. Podareanu, V. Codreanu, M. A. Veerman, M. Janssens, O. K. Hartogensis, and C. C. van Heerwaarden. Development of a large-eddy simulation subgrid model based on artificial neural networks: a case study of turbulent channel flow. *Geosci. Model Dev.*, 14(6):3769–3788, 2021.
- [37] S Stolz, NA Adams, and L Kleiser. An approximate deconvolution model for large-eddy simulation with application to incompressible wall-bounded flows. *Physics of Fluids*, 13(4):997–1015, 2001.
- [38] Amirhosein Toosi, Andrea G Bottino, Babak Saboury, Eliot Siegel, and Arman Rahmim. A brief history of ai: how to prevent another winter (a critical review). *PET clinics*, 16(4):449–469, 2021.
- [39] Kiwon Um, Robert Brand, Yun (Raymond) Fei, Philipp Holl, and Nils Thuerey. Solver-in-the-loop: Learning from differentiable physics to interact with iterative pde-solvers. In *Proceedings of the 34th International Conference on Neural Information Processing Systems*, Red Hook, NY, USA, 2020. Curran Associates Inc.
- [40] Oleg V Vasilyev. An adaptive version of the stretched-vortex subgrid-scale model for les on unstructured grids. *Journal of Computational Physics*, 173(1):139–164, 2001.
- [41] Oleg V. Vasilyev, Thomas S. Lund, and Parviz Moin. A general class of commutative filters for les in complex geometries. *J. Comput. Phys.*, 146(1):82–104, 1998.
- [42] Chenyue Xie, Jianchun Wang, and Weinan E. Modeling subgrid-scale forces by spatial artificial neural networks in large eddy simulation of turbulence. *Phys. Rev. Fluids*, 5:054606, May 2020.
- [43] Chenyue Xie, Jianchun Wang, Hui Li, Minping Wan, and Shiyi Chen. Artificial neural network mixed model for large eddy simulation of compressible isotropic turbulence. *Phys. Fluids*, 31(8), 2019.
- [44] Zhideng Zhou, Guowei He, Shizhao Wang, and Guodong Jin. Subgrid-scale model for large-eddy simulation of isotropic turbulent flows using an artificial neural network. *Comput. Fluids*, 195, 2019.